Batteries & Supercaps

Research Article
doi.org/10.1002/batt.202300519

Chemistry Europe
European Chemical Societies Publishing

www.batteries-supercaps.org

[4]Helicenium Ion as Bipolar Redox Material for Symmetrical Fully Organic Pole-less Redox Flow Battery

Jules Moutet,[a] David D. Mills,[a] Diego L. Lozier,[a] and Thomas L. Gianetti*[a]

Long duration storage batteries such as Redox Flow Batteries (RFBs) are promising storage system to address the energy storage requirement that our society will require in the years to come. Recent effort has been focused on the development of metal free and high energy density system such as all-organic non-aqueous redox flow batteries (NAORFBs). However high-voltage NAORFBs currently use distinct anolytes and catholytes, which are separated by a membrane sensitive to osmotic pressure, resulting in rapid capacity and energy density degradation over time. To address this issue, symmetric organic redox flow batteries (SORFBs) have been proposed as an elegant solution. We have introduced dimethoxyquinacridiniums ($DMQA^+$) ions as efficient bipolar redox molecules (BRMs) in static H-cell conditions. In this study, we present the first application of $DMQA^+$ ions in a complete flow RFB prototype, showcasing their ability to operate with polarity reversal. Key kinetic properties were evaluated through cyclic voltammetry and DFT calculations. While coulombic and energy efficiency metrics were moderate, pegylated $DMQA^+$ demonstrated impressive capacity retention of over 99.99% and the capability to operate under polarity inversion, making it a highly attractive choice for grid-scale, long-lifespan energy storage applications.

Introduction

To meet the energy transition of this century, our society relies on the increasing adoption of renewable energy sources.[1] However, despite the maturity and availability of solar and wind technologies, their intermittent nature makes it challenging to ensure consistent and reliable power.[2,3] The incorporation of efficient, inexpensive, and scalable Electrical Energy Storage (EES) systems has become crucial.[4–6] Among the various battery technologies in the ascending trend, Redox Flow Batteries (RFBs) represent a promising EES for large-scale stationary applications.[7–9] The decoupling of power and energy offers a greater engineering flexibility in RFBs design for integration into the electrical grid.

The existing commercially mature RFB technologies are mainly based on the stable redox states of transition metal ions (iron, chromium, vanadium) in Aqueous media (AqRFB).[10,11] Albeit other metal-based electrolytes have been documented in previous studies,[12–16] the extensive adoption of this categrory of AqRFB is hindered by various factors such as limited Energy Densities (E_d in Wh/L), concerns over the narrow electrochemical stability window of water (<1.5 V), ionic membrane separator expenses, compound toxicity, safety of handling large volumes of acid, and the significant geopolitical and environmental impact of mining ores.[17–19]

Non-aqueous RFBs present an attractive alternative[20] with the promise of higher energy density (electrochemical windows >5 V), eliminate the need for drastic pH conditions imposed by AqRFBs and enable the use of highly customizable Redox-active Organic Materials (ROMs).[21] This makes ROMs a preferable solution to metal ions since they can be sustainably synthesized, tailored to specific needs, and potentially produced from affordable raw materials.[14,22]

Most present-day Non-Aqueous fully-Organic RFBs (NAORFBs) adopt two ROMs for their posolyte and negolyte tanker, resulting in an asymmetric design that imposes rigorous selectivity features on the exchange membrane at the interface. The entropic diffusion of redox active material across the battery leads to irreversible capacity loss,[23] and induces new pathways for chemical degradation.[24] Various strategies to mitigate active material crossover has been promoted, such as implementing enhanced membrane formulation,[25,26] utilizing size exclusion techniques,[27,28] or incorporating immiscible electrolyte solutions.[29]

Inspired by the design of vanadium redox flow batteries (VRFBs), which use vanadium as the sole charge carrier on both sides of the cell, the development of Symmetrical Organic RFBs (SORFBs) has emerged the foremost choice for mitigating membrane crossover.[30] In the discharged state, the two poles of the battery contain a single Bipolar Redox-active Molecule (BRM)[31] that is capable of undergoing oxidation and reduction to enable the half-reactions of the anode and cathode, correspondingly. In the past few years, thanks to the adaptable nature of ROM designs, various categories of BRMs have emerged. A popular approach using the existing library of ROMs has achieved significant results by creating ambipolar compounds that link a donor redox unit to an appropriate acceptor redox moiety.[32–39] In comparison to this linking synthesis strategy providing closed-shell compound, several

[a] J. Moutet, D. D. Mills, D. L. Lozier, T. L. Gianetti
Department of Chemistry and Biochemistry
University of Arizona,
Tucson, AZ, 85719 United States
E-mail: tgianetti@arizona.edu

Supporting information for this article is available on the WWW under https://doi.org/10.1002/batt.202300519

Research Article
doi.org/10.1002/batt.202300519
Chemistry Europe
European Chemical Societies Publishing

stable organic radicals[40] with at least 2 redox electrochemical events have demonstrated impressive outcomes, notwithstanding their intrinsic heightened reactivity .[41–44]

In this growing field of SORFB, our research team has recently played a role in emphasizing the properties of helical carbenium ions, more specifically the [4]heliceniums ions dimethoxyquinacridiniums ($DMQA^+$).[45,46] Through the three stable redox states possessed by these carbocations, we were able to point out remarkable performances as electrolytic material for SORFB with E_{cell} voltages higher than 2.0 V. However our previous studies were only performed in a H-cell, the static RFB models.[33,47] Herein, we report the use of this DMQA platform in a flow RFB model for the first time. In this study we have also introduced polar glycol chain arms[31,48] in one step during the synthesis of $DMQA^+$ from the parent tris-aryl cation in order to improve the solubility of our material (Scheme 1). The resulting bench-stable compound [PEG-DMQA][BF_4] noted as $^{PEG}C^+$, with a promising theoretical E_d of 14.9 Wh/L, has been thoroughly investigated for its electrochemical behaviour. The outcome of this study unveils the deployment of a symmetrical RFB based on the DMQA carbocation platform, resulting in a near-perfect capacity retention (>99.9% /cycle) over 200 cycles in static H-Cell and over 180 cycles in a flow RFB set-up. Importantly, we also report the ability of our symmetrical system to operate within an alternating polarity mode in a so-called "pole-less" setup, while maintaining consistent capacity retention.[32,38,44]

Results and Discussion

Synthesis of $^{PEG}C^+$

The synthesis of the racemic 5,9-bis(3-(2-methoxyethoxy)propyl)-1,13-dimethoxy-5,9-dihydro-13bHquinolino[2,3,4-kl]acridin-13b-ylium tetrafluoroborate salt ($^{PEG}C^+$) has been investigated.[48] Tailoring moieties with polyethylene glycol chain has proved to be a relevant approach in the development of ROMs with increased solubility in NAORFB field.[49] The tunable and straightforward synthesis of [4]helicenium ions allowed a prompt implementation of this strategy.[50] To a solution of tris(2,6 dimethoxyphenyl)carbenium tetrafluoroborate salt[51] in acetonitrile, 10 equivalents of 3-(2-methoxyethoxy)propylamine were added. After a 24 h reflux, the acetonitrile was removed, and the green residue was extracted with CH_2Cl_2. The organic solution was washed with water until the aqueous layer became colorless. The desired compound was precipitated by addition of Et_2O to a concentrated solution in CH_2Cl_2. Crystals were obtained by layering Et_2O over a concentrated solution in CH_3CN to obtain $^{PEG}C^+$ as dark green blocks in a 66% yield (Scheme 1).

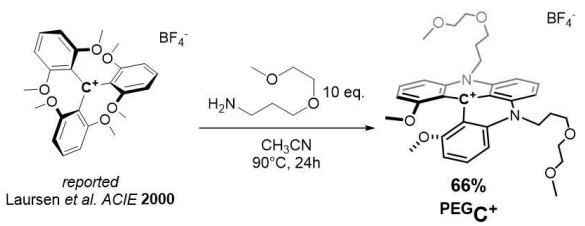

Scheme 1. Synthetic route for $^{PEG}C^+$ from tris(2,6 dimethoxyphenyl)carbenium tetrafluoroborate salt.

Electrochemical studies

In this investigation, acetonitrile was selected as the preferred solvent owing to its ability to stabilize the various oxidation states of $DMQA^+$,[45,46,52] its significant electrochemical window (~6.0 V), and its potential to enhance energy density.[42,53]

During cyclic voltammetry experiments in acetonitrile (0.5 M $TBABF_4$), $^{PEG}C^+$ exhibited three single-electron redox events (Figure 1). Half-wave potential of the reversible redox processes ($E_{1/2}$) were accurately acquired by Differential Pulse Voltammetry (DPV) experiments (Figure S5). A single-electron reduction is observed at $E_{1/2}^{Red} = -1.13$ V vs $AgNO_3$ and corresponds to the formation of the neutral radical $^{PEG}C^{\bullet}$ previously described.[54] Upon scanning to the cathodic region of potential, an oxidation event is observed at $E_{1/2}^{Ox} = 0.94$ V vs $AgNO_3$, corresponding to the formation of the dication radical $^{PEG}C^{\bullet++}$.[45] The event taking place at $E^{red2} = -1.98$ V vs $AgNO_3$ (Figure 1 DPV grey) is not reversible and will be discussed in the following.

In order to study the reversibility of these electronic processes, CVs were performed at different scan rates within the identical three-electrode setup (Figure 2). The graph in the bottom of Figure 2 demonstrates a linear correlation between the measured intensity (I) and the square root of the scan rate, suggesting unhindered electrolyte diffusion. Furthermore, both electronic processes exhibited full reversibility at all scan rates. The key kinetic parameters pertaining to electrochemical processes were extracted from these plots. Application of the Randles–Sevcik equation (Equation S1) yielded diffusion coefficient (D) values of 6.08×10^{-6} $cm^2.s^{-1}$ for both the $^{PEG}C^{\bullet++}/^{PEG}C^+$ and $^{PEG}C^+/^{PEG}C^{\bullet}$ pairs. These values signify efficient mass transport of the redox-active species from the bulk solution to the

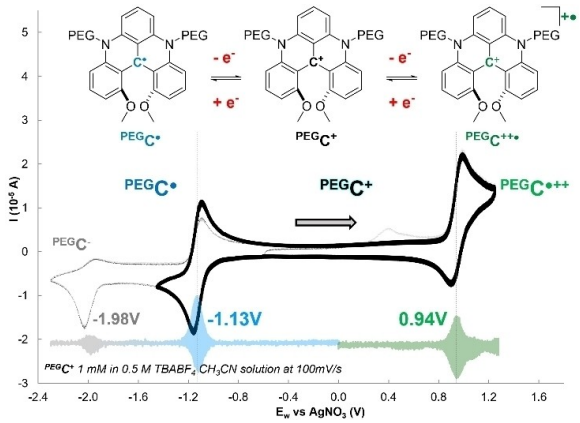

Figure 1. $^{PEG}C^+$ three stable oxidation states and CV of reversible events (black) and non-reversible event (grey) at of 100 mV s^{-1} at 1 mM in 0.5 M $TBABF_4$ CH_3CN solution. In pastel colour are depicted DPV in oxidation and reduction. Counter-cations and counter-anions omitted for clarity.

Research Article
doi.org/10.1002/batt.202300519

Chemistry Europe
European Chemical Societies Publishing

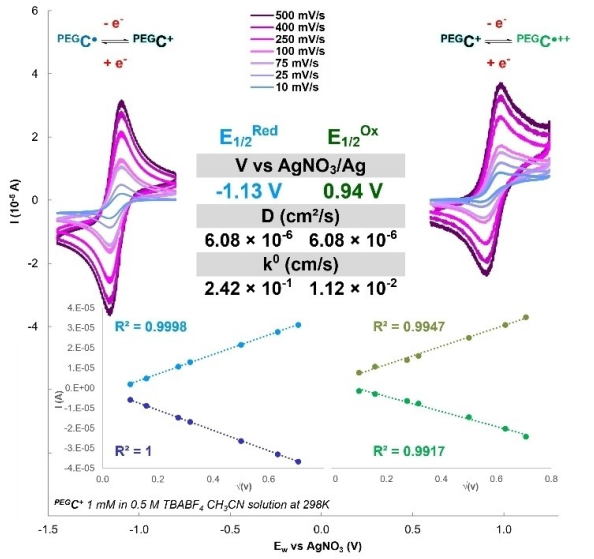

Figure 2. CV studies of $^{PEG}C^{+}$ (1 mM in 0.5 M $TBABF_4$ CH_3CN) with scan rates ranging from 10 to 500 $mV.s^{-1}$. Insert: depiction of anodic and cathodic peak current densities (I) in relation to the square root of the sweep rate ($v^{1/2}$) for the reduction (blue) and oxidation (green) processes. Table: summary of the obtained values $E_{1/2}$, D and k^0.

electrode surface, and they align with, or in some cases exceed, recent findings related to the use of ROMs for ORFBs application.[36,47,49,55–57]

Through the reported work of Lavagnini *et al.*, the electron transfer rate constant (k^0) has been determined (Equation S2-3).[58,59] The electronic process of $^{PEG}C^{+} \leftrightarrow {}^{PEG}C^{\bullet}$ exhibited a high value of $k^0 = 2.42\times10^{-1}$ $cm.s^{-1}$ while the oxidation path $^{PEG}C^{\bullet+} \leftrightarrow {}^{PEG}C^{+}$ appears slightly lower with a value $k^0 = 1.12\times10^{-2}$ $cm.s^{-1}$. This could be induced by the presence of the lone pair on the oxygen carried by the glycol arms. To verify if this is detrimental or will guarantee a good charge transfer reaction at the electrode surface, a 10 mM $^{PEG}C^{+}$ concentration study was performed (see Figure S8-11, S14 and Table S5). Although the electron transfer rates k^0 in the oxidative process is affected, these values remain within an acceptable range and are comparable to the redox shuttles published in the ORFB literature.[28,42,47,57] In addition, to provide a rapid estimation of the robustness of the $^{PEG}C^{+}/{}^{PEG}C^{\bullet}$ and $^{PEG}C^{\bullet+}/{}^{PEG}C^{+}$ each electronic event was subjected to cyclic testing within a three-electrode cell, resulting in the observation of minimal CV spectrum degradation over the course of 300 CV cycles (Figure S7 & S11).

This electrochemical investigation revealed that both the reversible reduction and oxidation processes could access the anticipated neutral radical and dicationic radical species associated with $DMQA^{+}$. Those three states of charges appeared reversible and are chemically stable on the time scale of CV experiments, demonstrating that $^{PEG}C^{+}$ satisfies the necessary criteria for its utilization as a BRM in SORFB.

Maximum E_d by solubility determination

The saturated concentration of $^{PEG}C^{+}$ in 0.5 M $TBABF_4$ in acetonitrile was evaluated by UV-Visible spectroscopy. A range of well-established concentrations standards were meticulously prepared and subsequently subjected to measurement, to determine the molar absorptivity (ε) at two distinct wavelengths: $\lambda_{max} = 432$ and 616 nm (Figure S15). The absorbance of a solution saturated with $^{PEG}C^{+}$ as subsequently assessed, employing three distinct dilution ratios (Figure S17) and applying the ε-values determined previously. The mean maximal concentration of $^{PEG}C^{+}$ in 0.5 M $TBABF_4$ dissolved in acetonitrile was determined to be 268 mM (Table S6).

The primary goal of ROM for RFBs is to achieve the maximum possible energy density (E_d), a parameter that can be defined as $E_d = nFE_{cell}C_{active}0.5$ (in $Wh.L^{-1}$).[14] In this formula, *n* represents the number of electrons involved in the redox process, *F* denotes the Faraday constant in A.h/L, E_{cell} which designates the voltage differential or potential gap between redox states ($E_{1/2}{}^{Ox} - E_{1/2}{}^{Red}$) and C_{active} denoting the concentration of redox-active species, a quantity equivalent to the electron concentration at both the cathode and anode. Through this equation for theoritical E_d of $^{PEG}C^{+}$ reaches a notable value of 14.9 $Wh.L^{-1}$ when accounting for an E_{cell} of 2.07 V and established C_{max} of 0.268 M. This places $^{PEG}C^{+}$ in the upper range of energy densities observed in most reported BRMs,[31] and it is 8 times higher compared to its alkyl parent (1.8 $Wh.L^{-1}$).[45] It is noteworthy that this pegylated carbenium ion approaches the energy density range observed in applied VRFB systems, which typically lie between 15 and 25 $Wh.L^{-1}$ at their best.[11]

DFT Calculations

After performing initial geometry optimizations in the gas phase and solvated phase, the molecular orbital (MO) energies [in eV] were graphed for the five different redox states calculated: $^{PEG}C^{+}$, $^{PEG}C^{+\bullet}$, $^{PEG}C^{\bullet}$ and $^{PEG}C^{-}$ (Figure S18). The calculations suggest straightforward reduction/oxidation of $^{PEG}C^{+}$ to $^{PEG}C^{\bullet}$ and $^{PEG}C^{+\bullet}$ respectively, as well as facile reduction of $^{PEG}C^{\bullet}$ to the anionic redox state $^{PEG}C^{-}$. While both the $^{PEG}C^{-\bullet}$ (triplet) and $^{PEG}C^{-}$ (singlet) denote plausible spin states, calculations suggest that the $^{PEG}C^{-}$ is more accessible. Consequently, the singlet description likely predominates as the principal contributing spin state to the anionic redox state. Given the highly reducing nature of the anionic species ($E = -1.98$ V vs $AgNO_3$), it is anticipated that the $^{PEG}C^{-}$ would be inclined to form byproducts if generated during charge-discharge cycling. Drawing from recorded CVs (Figure S12) and prior studies,[60,61] this anionic species has the ability to form, by proton abstraction, a neutral species DMQA–H (^{PEG}C–H, Figure S12) where a hydrogen is bound to the central carbon of the DMQA scaffold.

Since the solubility of different redox states cannot be explicitly calculated, it is beneficial to consider the relationship between experimental solubilities and free energies of

Research Article
doi.org/10.1002/batt.202300519
Chemistry Europe
European Chemical Societies Publishing

solvation.[62] More negative free energies of solvation are correlated to higher experimental solubilities, which offers a way to compare the relative experimental solubilities of different redox states.[63] The computations study suggests that the solubility trend, from highest to lowest, is $^{PEG}C^{+\bullet}$ > $^{PEG}C^{+}$ > $^{PEG}C^{\bullet}$ > ^{PEG}C-H (Table S7). $^{PEG}C^{\bullet}$ and ^{PEG}C–H are likely to be concerns when considering possible loss of capacity due to electrolyte precipitation. The impact of non-negligible ion solvation energy was taken into account for $^{PEG}C^{+}$ and $^{PEG}C^{+\bullet}$, and thus their free energy of solvation was computed as neutral salts with corresponding PF_6 counterions. Although there are substantial differences in the ΔG_{solv} values with and without counterions, the same solubility trend persists.

Galvanostatic Cycling with Potential Limitation

H-cell as "static-RFB"

The electrokinetic parameters of this new ROM, $^{PEG}C^{+}$, are promising and prompt us to first study the electrochemical reversibility and stability under static galvanostatic charge-discharge cycles in a static system. Bulk electrolysis charge/discharge cycling at 100% State of Charge (SOC) was carried out using an H-cell as a model for a redox flow cell setup. While this methodology cannot operate at high concentrations, studies have demonstrated that these types of electrochemical cell designs can serve as suitable test platforms for assessing the performance of organic redox-active materials in redox flow batteries.[28,33] Two different electrode setups were used depending on the concentration of the compound: i) 1 mM $^{PEG}C^{+}$, 3-electrode setup, reduction process at E_w with upper and lower voltage cutoffs of −1.55 V and −0.75 V., respectively *vs* E_{ref} (Figure 3); ii) 10 mM $^{PEG}C^{+}$, 2-electrode setup oxidation process at E_w with upper and lower voltage cutoffs of 2.3 V and 0 V, respectively *vs* E_{cell} (Figure 4).

To evaluate the capacity, efficiency, and stability of **1 mM** $^{PEG}C^{+}$ as a RFB ROM over multiple cycles, a total of 200 charge-discharge cycles were performed at |5| mA. The data presented in Figure 3(a) shows the results obtained between the 1st and 200th cycles. The initial charge-discharge cycle exhibited a medium capacity (Q) of 98.6% of the theoretical capacity, and a coulombic efficiency (CE) of 96.4%. Subsequently, the CE increased between the 2nd and 5th cycles to a steadily average value >99%, while the average Q retention remained consistent at 99.88% per cycle over the entire 200 cycles. Monitoring of the potential and the current at the E_w (Figure 3**(a)** insert) exhibits a regularity and a constant duration between each of the cycles in agreement with the good Q retention observed. The CV analysis of each chamber of the H-cell after 230 cycles, displayed in Figure 3(b) revealed that the E_w and E_c compartments were equally affected by the capacity fading. A decrease in CV area is noted with the $^{PEG}C^{\bullet+}\leftrightarrow{}^{PEG}C^{+}$ process losing resolution. A slight shoulder corresponding to an irreversible peak at 0.51 V vs $AgNO_3$ also appears for each of the solutions. Local overloads capable of generating the $^{PEG}C^{-}$ that abstract H are responsible for the presence of this peak characteristic of ^{PEG}**C-H** (observed in the CV characterization of the compound in Figure 1).[60,61] These results in a symmetrical cell at 1 mM have motivated the studies at a higher concentration.

The stability of **10 mM** $^{PEG}C^{+}$ as a BRM was evaluated during 100 charge-discharge cycles where E_w proceeded to the $^{PEG}C^{\bullet+}$ /$^{PEG}C^{+}$ transformation. We also chose to switch to a 2-electrode system, similar to that of an in-flow RFB cell. The whole test was performed at |6.7| mA. The data collected between the first and the 100th cycles are shown in Figure 4(a). During the initial charge-discharge cycle, the average Q was 59.7% of the theoretical capacity, and the CE value was 71.8%. However, in

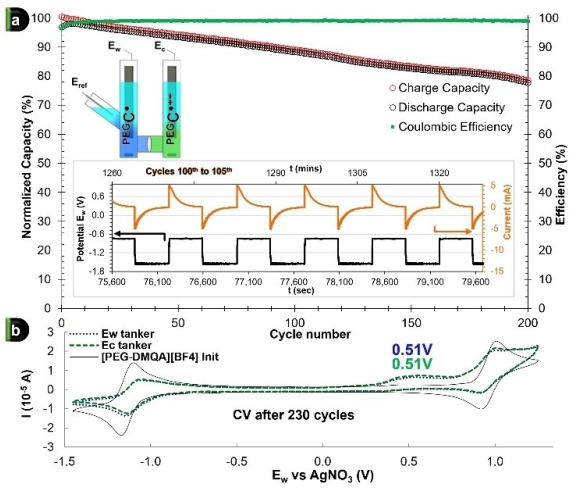

Figure 3. (a) Plot of charge, discharge capacity (normalized to theoretical capacity) and coulombic efficiency vs cycle number for H-cell cycling of **1 mM** $^{PEG}C^{+}$ in a 3-electrode setup at |5| mA for 200 cycles ~43 h. Each data point represents one cycle. Insert: monitoring of E_w and I vs time for cycles 100 to 105. (b) CVs of tanker solutions after 230 cycles (>48 h) and comparison with initial $^{PEG}C^{+}$ CV.

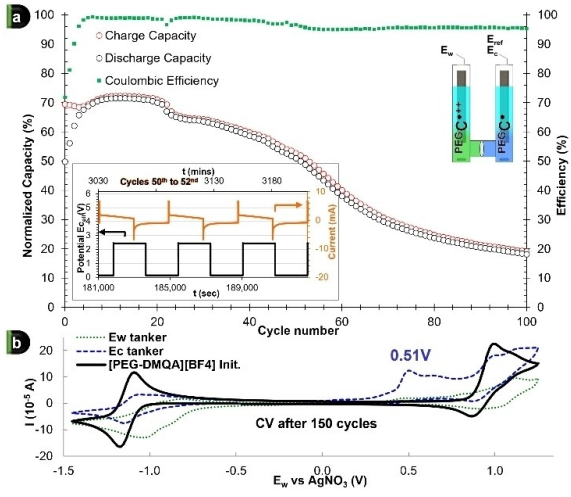

Figure 4. (a) Plot of charge, discharge capacity (normalized to theoretical capacity) and coulombic efficiency vs cycle number for H-cell cycling of **10 mM** $^{PEG}C^{+}$ in a 2-electrode setup at |6.7| mA for 100 cycles ~102 h. Each data point represents one cycle. Insert: monitoring of E_w and I vs time for cycles 50 to 52. (b) CVs of tanker solutions after 150 cycles (>149 h) and comparison with initial $^{PEG}C^{+}$ CV.

the subsequent cycles (2nd to 5th), the CE increased to an average value close to 97%, while the average Q retention remained constant at 99.4% per cycle throughout the 100 cycles. The potential and current monitoring at E_w (as shown in Figure 4(a) insert) exhibited a consistent pattern and duration between each cycle, supporting the observed good Q retention. However, after 150 cycles, an analysis of the CV of each chamber of the H-cell (as shown in Figure 4(b)) revealed that the E_w and E_c compartments had significant decay. The resolution of the CV's shape was lost, and while the oxidation process (E_w compartment) showed only fatigue signs through a loss of area, the E_c where the reduction occurs ($^{PEG}\mathbf{C}^+ \leftrightarrow {}^{PEG}\mathbf{C}^\bullet$) presents a massive peak at +0.51 V vs $AgNO_3$ characteristic of the formation of $^{PEG}\mathbf{C}$–**H**. This feature is indicative of intense overload at the E_c side of the H-cell allowing the formation of $^{PEG}\mathbf{C}^-$, directly related to the absence of flow in the H-Cell setup and diffusion-driven of the species. These results, along with the loss of capacity due to physical phenomena and the static aspect of the electrolyte, motivated a full flow study.

Full Redox Flow cell

To better evaluate the performance in a full-RFB, $^{PEG}\mathbf{C}^+$ was deployed in a fully symmetric organic redox flow battery cell prototype (Figure S3). Unlike the H-cell cycling, this experiment used a polymer-based exchange membrane instead of the ultra-fine glass sinter separator and the previously used RVC electrodes were replaced by carbon felt electrodes deployed within commercially available RFB solutions. Nevertheless, complete in-flow battery cycling presented additional challenges compared to charge-discharge cycling in a static H-cell, primarily owing to the presence of multiple hardware components, including tubing, bipolar plates, electrodes, and separator membranes (Figure S3), which all interacted with the redox-active molecules bearing a radical charge. Furthermore, the circulation of the electrolyte within the cell and the tanks, coupled with the potential crossover of "anolyte" and "posolyte" between the two pole of the cell during flow cycling, may lead to self-discharge and a reduction in capacity retention when compared to what is observed in a static H-cell.

To address these challenges, the flow cell was configured utilizing bipolar graphite plates equipped with a serpentine flow pattern, along with carbon-felt electrodes (Sigracet 29 AA) measuring 400 μm in thickness. These electrodes possess an 80% porosity and exhibit an electrical resistivity of under 5 $m\Omega.cm^2$. An in-depth analysis was conducted to investigate the surface chemistry of the electrodes in the existing literature and was found to be suitable for the development of NAORFB.[64] The two side of the cell were separated by a Daramic-175 porous membrane as exchange separator for the counter anions. During galvanostatic cycling the electrolyte solutions flowed through the cell at 16 mL/min. Recent techno-economic analyses have set an area-specific resistance (ASR) target of less than 5 Ω/cm^2 to improve NAqORFB design.[65] In order to qualify our prototype for upscaling, potential electrochemical impedance spectroscopy (PEIS) at 0% SOC (when the SORFB is at equilibrium, $^{PEG}\mathbf{C}^+/{}^{PEG}\mathbf{C}^+$) before and after cycling has been performed. Charging and discharging were conducted at a constant current rate equivalent to 2 C-rate until a voltage cutoff of +200 mV from the cell's theoretical E_{gap} of 2.1 V was reached, with a 90% state of charge (SOC) limit applied. The discharge cutoff was set at 0 V, corresponding to 0% SOC. At the interface, the charges generated on the BRM were compensated by the migration of BF_4^- counter anions through the permeable exchange membrane (Figure 5(a)). A **1 mM** $^{PEG}\mathbf{C}^+$ electrolyte solution with 0.5 M $TBABF_4$ in acetonitrile was flowed through the cell at 8 mL/min per tanker, in a 2-electrode setup with the reduction process at the E_w ($E_w = -$, Figure 5(**a**)) and a maximum SOC of 90%). In this test, the SORFB had been cycled 75 times (i.e. ~60 h) and a consistent retention of capacity, with an average discharge capacity and coulombic efficiency (CE) of 68% were recorded (Figure 5(**b**)). Despite charging the battery to its full normalized capacity, the poor CE observed is directly related to the observed energy efficiency inferior to 50% (45% over 75 cycles). This suggests a loss of energy between the charged state and the discharge sequence, partially attributable to self-discharge. Meanwhile, after cycle 5, the discharge capacity is almost constant with an average loss of 0.0004%/cycle underlining the sturdiness of $^{PEG}\mathbf{C}^+$ as charge carrier. The data of both the potential and current of the RFB cell, as illustrated in the Figure 5(b) insert, demonstrated constant cycle duration. This observation correlates with the good Q retention. The potential electrochemical impedance spectroscopy (PEIS) of the cell in flow before and after cycling (at 0% SOC) with an ASR of 0.58 Ω before cycling and a similar value of 0.59 Ω after 75 cycles (Figure 5(**c**)) illustrated the robustness of the system, and the absence of irreversible reactions at the interface. It is probable that pegylated $DMQA^+$ and its charged states undergo an energetically costly conformational change rather than an irreversible chemical transformation, which protects it from rapid capacity fade. It is worth noting that after 75 cycles, the cyclic voltammograms of each tanker recorded in a 3-electrode cell show no significant loss in area, even though the posolyte ($^{PEG}\mathbf{C}^+ \leftrightarrow {}^{PEG}\mathbf{C}^{\bullet++}$) appears to have lost some resolution (Figure 5(d)).

To demonstrate the inherent feature of SORFB's innovative pole-less battery design and its safe charging ability regardless of polarization, we conducted an additional cycling experiment where the SORFB could be charge positively at the working electrode ($E_w = +$, (Figure 5(e)). The battery, containing **1 mM** of $^{PEG}\mathbf{C}^+$ in 0.5 M $TBABF_4$, underwent 90 cycles of "anolyte" charging ($E_w = -$), followed by 18 polarity reversal every 5 cycles for a total of 180 cycles ((Figure 5(f) & (g)). The initial 90 cycles aligned with the preceding experiment, yielding the same 68% CE and discharge capacity, while maintaining an average of 45% EE. Upon reversing the polarity at the 91st cycle, as observed earlier, a 100% charge capacity was reached, followed by a sudden decrease in discharge capacity (48%), CE (29%), and EE (33%). However, within just 5 cycles under the same polarity, the battery swiftly returned to the exact CE, EE and capacity values observed before under "anolyte" charging, highlighting the regeneration of its initial characteristics. This phenomenon persisted through the 18 inversions applied to

Research Article
doi.org/10.1002/batt.202300519
Chemistry Europe
European Chemical Societies Publishing

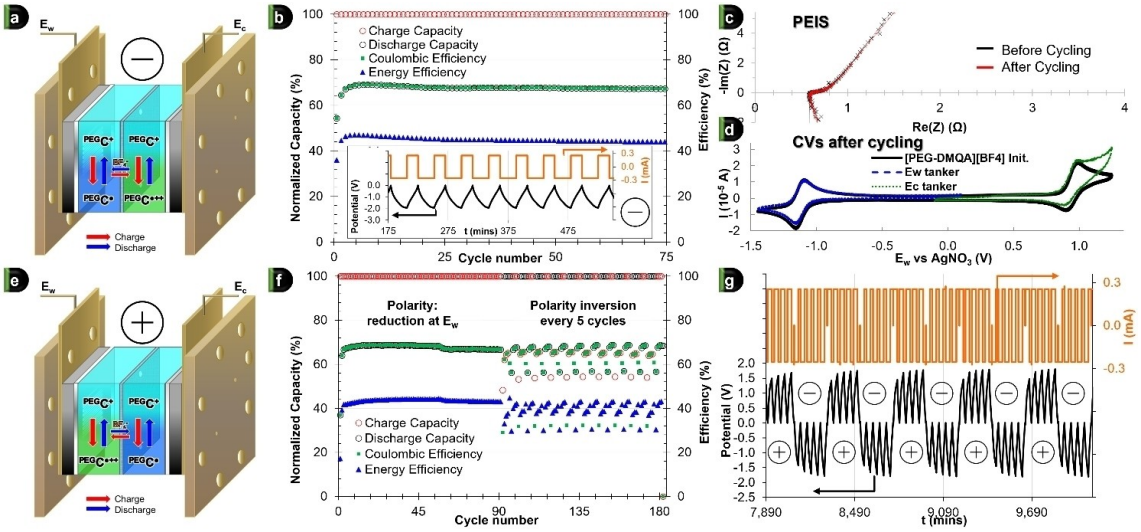

Figure 5. (a) Scheme of the SORFB cell during "anolyte" cycling −. (b) Plot of charge, discharge capacity (normalized), coulombic efficiency and energy efficiency vs cycle number for RFB-cell cycling with tankers loaded each with 4 mL of **1 mM $^{PEG}C^{+}$**, flow 8 mL/min per channel, 2 C-rate for 75 cycles ~60 h. Each data point represents one cycle. Insert: monitoring of cell potential and I vs times for cycles 4 to 11. (c) Potential Electrochemical Impedance Spectroscopy (PEIS) of the cell in flow before and after 75 cycles (both at 0% SOC) from 1Ghz to 0.1 Hz with an amplitude of 10 mV. (d) CVs of tanker solutions after 75 cycles (60 h) and comparison with initial $^{PEG}C^{+}$ CV. (e) Scheme of the SORFB cell during "catholyte" cycling +. (f) Plot of charge, discharge capacity (normalized), coulombic efficiency and energy efficiency vs cycle number for pole-less RFB-cell cycling with tankers loaded each with 4 mL of 1 mM $^{PEG}C^{+}$, flow 8 mL/min per channel, 2 C-rate for 180 cycles ~145 h. Each data point represents one cycle. (g) Monitoring of cell potential and I *vs* times for 10 inversion of polarity (cycles 91 to 140).

the battery. The discharge capacity of the BRM remained unaffected, displaying an average capacity retention of >99.99% throughout the entire experiment and even through successive polarity reversals, underscoring the outstanding durability of this ROM and opens the door to his use in pole-less RFBs.

Conclusions

This study demonstrates the $DMQA^{+}$ platform is a robust and promising bipolar material for SORFBs. The cyclic voltammetry and cell cycling studies in CH_3CN solution revealed high electrochemical reversibility and chemical stability, highlighting the good performance of this scaffold design. The various concentration cycling tests, carried out in both static and flow cells, and the first-ever demonstration of the use of $DMQA^{+}$ in full flow RFB, showcased the potential of this technology in the development of high-performance SORFBs. Indeed, albeit exhibiting moderate CE (68%) and EE (45%) values, the in-flow experiments demonstrated a capacitance retention of over 99.99%, even in a "pole-less" configuration with 18 successive polarization inversions. This specific experiment also emphasized the resilience of the $DMQA^{+}$ platform and its ability to undergo pole-less charging and discharging. This work provides a proof of concept for the use of carbenium class bipolar redox scaffolds in full flow pole-less RFB, representing a step towards developing innovative all-organic, symmetrical RFB. Further work is currently performed to investigate the long-term stability, higher concentrations and current density accessible in operational conditions.

Supporting Information

Experimental details; NMR spectra; Single X-ray diffraction; Electrochemical Investigations details; cell architectures; UV-Visible plot and max concentration; DFT SOMO-LUMO and calculated solvation free energy; and SORFBs cycling data are available in online Supporting Information.

Acknowledgements

We are grateful to the University of Arizona, Salt River Project (Phoenix, AZ) and Research Corporation for Science Advancement Cottrell Scholarship 2021 (Award #27536) for financially supporting this work. We thank Dr. Andrei Astashkin (XRD facility of the University of Arizona, RRID:SCR_022886) for his help with XRD data collection and analysis. The purchase of the diffractometer was funded by the National Science Foundation under grant number 0741837. All NMR data were collected in the NMR facility of the Department of Chemistry and Biochemistry at the University of Arizona, RRID:SCR_012716. The purchase of the Bruker NEO 500 MHz spectrometer was supported by the National Science Foundation under Grant Number 1920234 and the University of Arizona.

Conflict of Interests

The authors declare no conflict of interest.

Research Article
doi.org/10.1002/batt.202300519
Chemistry Europe
European Chemical Societies Publishing

Data Availability Statement

The data that support the findings of this study are available from the corresponding author upon reasonable request.

Keywords: nonaqueous redox flow battery · bipolar molecule · energy storage · electrolyte design · helical carbenium •

[1] M. S. Dresselhaus, I. L. Thomas, *Nature* **2001**, *414*, 332–337.
[2] J. Rugolo, M. J. Aziz, *Energy Environ. Sci.* **2012**, *5*, 7151–7160.
[3] M. S. Ziegler, J. M. Mueller, G. D. Pereira, J. Song, M. Ferrara, Y. Chiang, J. E. Trancik, *Joule* **2019**, *3*, 2134–2153.
[4] Z. Yang, J. Zhang, M. C. W. Kintner-Meyer, X. Lu, D. Choi, J. P. Lemmon, J. Liu, *Chem. Rev.* **2011**, *111*, 3577–3613.
[5] S. P. S. Badwal, S. S. Giddey, C. Munnings, A. I. Bhatt, A. F. Hollenkamp, *Front. Chem.* **2014**, *2*, 1–28.
[6] T. M. Gür, *Energy Environ. Sci.* **2018**, *11*, 2696–2767.
[7] B. Dunn, H. Kamath, J.-M. Tarascon, *Science* **2011**, *334*, 928–935.
[8] P. Alotto, M. Guarnieri, F. Moro, *Renewable Sustainable Energy Rev.* **2014**, *29*, 325–335.
[9] E. Sánchez-Díez, E. Ventosa, M. Guarnieri, A. Trovò, C. Flox, R. Marcilla, F. Soavi, P. Mazur, E. Aranzabe, R. Ferret, *J. Power Sources* **2021**, *481*, 228804.
[10] Y. K. Zeng, T. S. Zhao, L. An, X. L. Zhou, L. Wei, *J. Power Sources* **2015**, *300*, 438–443.
[11] K. Lourenssen, J. Williams, F. Ahmadpour, R. Clemmer, S. Tasnim, *J. Energy Storage* **2019**, *25*, 100844.
[12] P. J. Cabrera, X. Yang, J. A. Suttil, K. L. Hawthorne, R. E. M. Brooner, M. S. Sanford, L. T. Thompson, *J. Phys. Chem. C* **2015**, *119*, 15882–15889.
[13] J. A. Suttil, J. F. Kucharyson, I. L. Escalante-Garcia, P. J. Cabrera, B. R. James, R. F. Savinell, M. S. Sanford, L. T. Thompson, *J. Mater. Chem. A* **2015**, *3*, 7929–7938.
[14] J. Winsberg, T. Hagemann, T. Janoschka, M. D. Hager, U. S. Schubert, *Angew. Chem. Int. Ed.* **2017**, *56*, 686–711.
[15] E. S. Beh, D. De Porcellinis, R. L. Gracia, K. T. Xia, R. G. Gordon, M. J. Aziz, *ACS Energy Lett.* **2017**, *2*, 639–644.
[16] M. Park, E. S. Beh, E. M. Fell, Y. Jing, E. F. Kerr, D. Porcellinis, M. Goulet, J. Ryu, A. A. Wong, R. G. Gordon, J. Cho, M. J. Aziz, *Adv. Energy Mater.* **2019**, *9*, 1900694.
[17] DOE Office of ARPR–E. ARPA–E, "GRIDS Program Overview," **2011**.
[18] U. S. DEPARTMENT OF HEALTH AND HUMAN SERVICES Public Health Service Agency for Toxic Substances and Disease Registry, in *ATSDR's Toxicol. Profiles*, CRC Press, **2012**.
[19] R. M. Wittman, M. L. Perry, T. N. Lambert, B. R. Chalamala, Y. Preger, *J. Electrochem. Soc.* **2020**, *167*, 090545.
[20] Z. Rhodes, J. R. Cabrera-Pardo, M. Li, S. D. Minteer, *Isr. J. Chem.* **2021**, *61*, 101–112.
[21] L. Kortekaas, S. Fricke, A. Korshunov, I. Cekic-Laskovic, M. Winter, M. Grünebaum, *Batteries* **2022**, *9*, 4.
[22] Y. Ding, C. Zhang, L. Zhang, Y. Zhou, G. Yu, *Chem. Soc. Rev.* **2018**, *47*, 69–103.
[23] M. L. Perry, J. D. Saraidaridis, R. M. Darling, *Curr. Opin. Electrochem.* **2020**, *21*, 311–318.
[24] A. Shrestha, K. H. Hendriks, M. S. Sigman, S. D. Minteer, M. S. Sanford, *Chem. A Eur. J.* **2020**, *26*, 5369–5373.
[25] M. T. Tsehaye, G. Mourouga, T. J. Schmidt, J. O. Schumacher, S. Velizarov, B. Van der Bruggen, F. Alloin, C. Iojoiu, *Renewable Sustainable Energy Rev.* **2023**, *173*, 113059.
[26] B. H. Robb, T. Y. George, C. M. Davis, Z. Tang, C. H. Fujimoto, M. J. Aziz, M. P. Marshak, *J. Electrochem. Soc.* **2023**, *170*, 030515.
[27] S. E. Doris, A. L. Ward, A. Baskin, P. D. Frischmann, N. Gavvalapalli, E. Chénard, C. S. Sevov, D. Prendergast, J. S. Moore, B. A. Helms, *Angew. Chem. Int. Ed.* **2017**, *56*, 1595–1599.
[28] K. H. Hendriks, S. G. Robinson, M. N. Braten, C. S. Sevov, B. A. Helms, M. S. Sigman, S. D. Minteer, M. S. Sanford, *ACS Cent. Sci.* **2018**, *4*, 189–196.
[29] P. Navalpotro, N. Sierra, C. Trujillo, I. Montes, J. Palma, R. Marcilla, *ACS Appl. Mater. Interfaces* **2018**, *10*, 41246–41256.
[30] R. A. Potash, J. R. McKone, S. Conte, H. D. Abruña, *J. Electrochem. Soc.* **2016**, *163*, A338–A344.
[31] M. Li, J. Case, S. D. Minteer, *ChemElectroChem* **2021**, *8*, 1215–1232.
[32] T. Janoschka, C. Friebe, M. D. Hager, N. Martin, U. S. Schubert, *ChemistryOpen* **2017**, *6*, 216–220.
[33] P. W. Antoni, T. Bruckhoff, M. M. Hansmann, *J. Am. Chem. Soc.* **2019**, *141*, 9701–9711.
[34] N. H. Attanayake, J. A. Kowalski, K. V. Greco, M. D. Casselman, J. D. Milshtein, S. J. Chapman, S. R. Parkin, F. R. Brushett, S. A. Odom, *Chem. Mater.* **2019**, *31*, 4353–4363.
[35] V. V. Sentyurin, O. A. Levitskiy, T. V. Magdesieva, *Curr. Opin. Electrochem.* **2020**, *24*, 6–14.
[36] P. Geysens, Y. Li, I. Vankelecom, J. Fransaer, K. Binnemans, *ACS Sustainable Chem. Eng.* **2020**, *8*, 3832–3843.
[37] J. S. Tracy, E. S. Horst, V. A. Roytman, F. D. Toste, *Chem. Sci.* **2022**, *13*, 10806–10814.
[38] Y. Liu, G. Dai, Y. Chen, R. Wang, H. Li, X. Shi, X. Zhang, Y. Xu, Y. Zhao, *ACS Energy Lett.* **2022**, *7*, 1274–1283.
[39] B. I. Loomans, S. E. Bottle, J. P. Blinco, *Batteries & Supercaps* **2023**, *6*, e202200561.
[40] C. G. Armstrong, K. E. Toghill, *Electrochem. Commun.* **2018**, *91*, 19–24.
[41] T. Hagemann, J. Winsberg, B. Häupler, T. Janoschka, J. J. Gruber, A. Wild, U. S. Schubert, *NPG Asia Mater.* **2017**, *9*, e340–e340.
[42] A. Korshunov, M. J. Milner, M. Grünebaum, A. Studer, M. Winter, I. Cekic-Laskovic, *J. Mater. Chem. A* **2020**, *8*, 22280–22291.
[43] V. V. Sentyurin, O. A. Levitskiy, T. V. Magdesieva, *Curr. Opin. Electrochem.* **2020**, *24*, 15–23.
[44] J. S. Steen, J. L. Nuismer, V. Eiva, A. E. T. Wiglema, N. Daub, J. Hjelm, E. Otten, *J. Am. Chem. Soc.* **2022**, *144*, 5051–5058.
[45] J. Moutet, J. M. Veleta, T. L. Gianetti, *ACS Appl. Energ. Mater.* **2021**, *4*, 9–14.
[46] J. Moutet, D. Mills, M. M. Hossain, T. L. Gianetti, *Mater Adv* **2022**, *3*, 216–223.
[47] Y. Yan, S. G. Robinson, M. S. Sigman, M. S. Sanford, *J. Am. Chem. Soc.* **2019**, *141*, 15301–15306.
[48] N. Bisballe, B. W. Laursen, *Chem. A Eur. J.* **2020**, *26*, 15969–15976.
[49] J. Chai, A. Lashgari, Z. Cao, C. K. Williams, X. Wang, J. Dong, J. "Jimmy" Jiang, *ACS Appl. Mater. Interfaces* **2020**, *12*, 15262–15270; Jiang, *ACS Appl. Mater. Interfaces* **2020**, *12*, 15262–15270.
[50] J. Bosson, N. Bisballe, B. W. Laursen, J. Lacour, *Cationic Triarylcarbenium Helicenes: Synthesis, Resolution, and Applications*, Wiley, **2022**.
[51] B. W. Laursen, F. C. Krebs, *Angew. Chem.* **2000**, *39*, 3432–3434.
[52] L. Mei, J. M. Veleta, T. L. Gianetti, *J. Am. Chem. Soc.* **2020**, *142*, 12056–12061.
[53] K. Gong, Q. Fang, S. Gu, S. F. Y. Li, Y. Yan, *Energy Environ. Sci.* **2015**, *8*, 3515–3530.
[54] A. C. Shaikh, J. Moutet, J. M. Veleta, M. M. Hossain, J. Bloch, A. V. Astashkin, T. L. Gianetti, *Chem. Sci.* **2020**, *11*, 11060–11067.
[55] X. Xing, Q. Liu, W. Xu, W. Liang, J. Liu, B. Wang, J. P. Lemmon, *ACS Appl. Energ. Mater.* **2019**, *2*, 2364–2369.
[56] Y. Yan, T. P. Vaid, M. S. Sanford, *J. Am. Chem. Soc.* **2020**, *142*, 17564–17571.
[57] L. Zhang, Y. Qian, R. Feng, Y. Ding, X. Zu, C. Zhang, X. Guo, W. Wang, G. Yu, *Nat. Commun.* **2020**, *11*, 3843.
[58] R. S. Nicholson, *Anal. Chem.* **1965**, *37*, 1351–1355.
[59] I. Lavagnini, R. Antiochia, F. Magno, *Electroanalysis* **2004**, *16*, 505–506.
[60] D. Conreaux, N. Mehanna, C. Herse, J. Lacour, *J. Org. Chem.* **2011**, *76*, 2716–2722.
[61] T. J. Sørensen, M. F. Nielsen, B. W. Laursen, *ChemPlusChem* **2014**, *79*, 1030–1035.
[62] G. Duarte Ramos Matos, D. Y. Kyu, H. H. Loeffler, J. D. Chodera, M. R. Shirts, D. L. Mobley, *J. Chem. Eng. Data* **2017**, *62*, 1559–1569.
[63] S. Dasari, B. S. Mallik, *J. Mol. Liq.* **2020**, *301*, 112449.
[64] K. V. Greco, A. Forner-Cuenca, A. Mularczyk, J. Eller, F. R. Brushett, *ACS Appl. Mater. Interfaces* **2018**, *10*, 44430–44442.
[65] J. D. Milshtein, J. L. Barton, T. J. Carney, J. A. Kowalski, R. M. Darling, F. R. Brushett, *J. Electrochem. Soc.* **2017**, *164*, A2487–A2499.

Manuscript received: November 7, 2023
Revised manuscript received: January 3, 2024
Accepted manuscript online: January 5, 2024
Version of record online: January 22, 2024